

Microwave radiative transfer model validation

Philip W. Rosenkranz¹ and Christopher D. Barnet²

Received 22 March 2005; revised 27 June 2005; accepted 20 July 2005; published 11 March 2006.

[1] Within the geophysical retrieval algorithm for AIRS/AMSU/HSB, a forward radiative transfer model is used to calculate microwave brightness temperatures. Components of the microwave forward model include a surface emissivity model, the influence of surface scattering characteristics on reflected downwelling emission from the atmosphere, and an atmospheric transmittance model. Over the ocean, the surface model parameters are shown to be related to near-surface wind speed. Calculations using the atmospheric transmittance model with profiles from dedicated radiosondes launched underneath the Aqua satellite show good agreement with HSB measurements.

Citation: Rosenkranz, P. W., and C. D. Barnet (2006), Microwave radiative transfer model validation, *J. Geophys. Res.*, **111**, D09S07, doi:10.1029/2005JD006008.

1. Introduction

[2] The Atmospheric Infrared Sounder (AIRS), the Advanced Microwave Sounding Unit-A (AMSU-A) and the Humidity Sounder for Brazil (HSB) instruments on the Aqua satellite compose an advanced atmospheric sounding facility [Aumann *et al.*, 2003]. The geophysical parameter retrieval algorithm for AIRS/AMSU/HSB incorporates forward radiative transfer models to compute radiances or brightness temperatures from current iteration values of inferred atmospheric and surface parameters. Even for the purpose of atmospheric sounding alone, having the correct boundary condition at the surface is necessary for the forward calculation. The prelaunch version of the microwave forward model was described by Rosenkranz [2003, hereinafter R03]. R03 also tested the algorithm by comparison to measurements made by the NOAA 15 AMSU-A. This paper addresses two further aspects of the forward model (version 4.0): postlaunch revisions to the microwave surface model and its sensitivity to ocean surface wind speed; and second, validation for HSB channels.

[3] The microwave forward model consists of a parameterized algorithm to compute atmospheric transmittance, a model for surface brightness temperature, and models for approximation of the reflected downwelling atmospheric emission, which depends on the surface scattering characteristics. The transmittance algorithm has undergone only minor updating from R03, with recent measurements [Tretyakov *et al.*, 2003] of parameters in the line-by-line absorption models from which it is derived. In contrast, the components related to the surface have been extensively revised since the launch of Aqua, on the basis of experi-

ence with the microwave data, and these components are described in detail in the next two sections. Sections 4 and 5 describe the tests performed to validate the model's components. These tests were done using Aqua data during the time period when HSB was operational, which was June 2002 through January 2003.

2. Surface Brightness Temperature Model

[4] From a physical point of view, one usually thinks of surface temperature and surface emissivity as separate variables; however, the retrieval algorithm treats the product of emissivity and temperature, denoted as surface brightness temperature T_{SB} , as an independent variable because this product is closely related to the window channel measurements. Surface skin temperature is retrieved along with air temperature, with which it is correlated, from a different set of channels. Hence we write the equation of radiative transfer in the form:

$$T_B = T_{Bdirect} + \tau [T_{SB} + T_{Bsky}(1 - T_{SB}/T_s)], \quad (1)$$

where T_B is the upward propagating brightness temperature from the top of the atmosphere, $T_{Bdirect}$ is the atmospheric contribution of the direct path from surface footprint to satellite and τ is the atmospheric transmittance along that path, T_s is the surface skin temperature, and T_{Bsky} is the downward propagating sky brightness temperature, calculated as discussed in the next section. The cosmic background contribution is included in T_{Bsky} .

[5] The first step in calculation of surface brightness temperature is a classification of the footprint as having one of eight types of surface. The classification algorithm, which uses AMSU-A channels 1, 2, 3, and 15 (23.8, 31.4, 50.3, 89.0 GHz), differs from that described in R03, which used the discriminant functions of Grody *et al.* [2000], mainly by the addition of another snow type. We assign to each surface type an a priori emissivity spectrum $\epsilon_0(\nu)$, plotted versus frequency ν in Figure 1. However,

¹Research Laboratory of Electronics, Massachusetts Institute of Technology, Cambridge, Massachusetts, USA.

²National Environmental Satellite Data and Information Service, NOAA, Camp Springs, Maryland, USA.

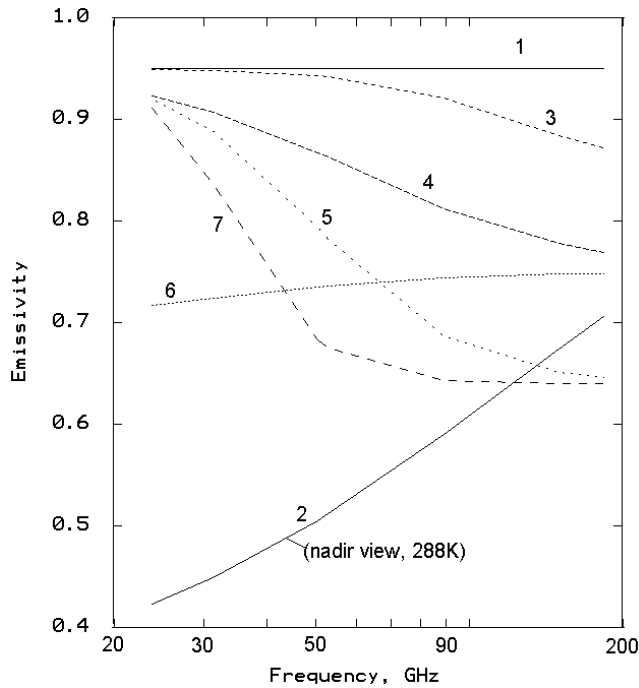


Figure 1. A priori emissivities $\epsilon_0(\nu)$ of surface types listed in Table 1. The emissivity of water depends on temperature and incidence angle. Coastline emissivities are computed as mixtures of land and water.

because surface emissivity varies, the retrieval is allowed to adjust the surface brightness spectrum in order to fit the observations. (Alternative approaches are illustrated by *Weng et al.* [2001], who calculated emissivity from a physical model, and by *Karbou et al.* [2005], who derived a database of surface emissivity from AMSU measurements, to be used as a priori information for a retrieval algorithm.)

[6] The retrieval of surface brightness is combined with the atmospheric moisture profile retrieval, using channels 1, 2, 3, and 15 of AMSU-A, and all four HSB channels (150, 183.3 ± 1 , ± 3 , ± 7 GHz). If emissivity were allowed to vary independently at each frequency that penetrates to the surface, there would be too many degrees of freedom to solve the problem. The number of degrees of freedom can be reduced either by assuming correlations among the emissivities at different frequencies, or by using an analytic function of frequency with a small number of free parameters to represent the frequency dependence. We chose the

latter method. Thus surface brightness temperature is represented as a function of frequency ν by

$$T_{SB}(\nu) = \epsilon_0(\nu)T_{S0} + T_0 + T_1F_1(\nu) + T_2F_2(\nu) \quad (2)$$

where T_{S0} is the a priori (climatological) surface temperature, the parameters T_0 , T_1 , and T_2 allow the retrieval solution to adjust the spectrum (they have a priori values of zero), and

$$F_1(\nu) = \nu^s / (\nu^s + \nu_1^s), \quad (3a)$$

$$F_2(\nu) = \nu^s / (\nu^s + \nu_2^s). \quad (3b)$$

The coefficients ν_1 , ν_2 and s are assigned according to surface type, as in Table 1. $F_1(\nu)$ and $F_2(\nu)$ both increase with frequency from zero to unity; see the examples in Figure 2. Thus ν_1 and ν_2 are transition frequencies between three frequency bands which, when ν_1 and ν_2 are widely spaced and s is relatively large, have surface brightness temperatures that differ from the a priori spectrum approximately by T_0 , $T_0 + T_1$, and $T_0 + T_1 + T_2$, respectively. For the frozen surfaces in Table 1, the value $s = 3$ makes the transitions between the three frequency bands sufficiently rapid that their surface brightness temperatures can be independently adjusted in the retrieval.

[7] For water, coastline and land footprints, the variance of T_2 is set to zero; therefore the a posteriori value of T_2 remains zero, and (2) becomes equivalent to equation (8) in R03 with the substitution $T_\infty = T_0 + T_1$. T_0 and T_∞ are then the low- and high-frequency asymptotes of the surface brightness adjustment. The values $s = 1.2$ and $\nu_1 = 90$ GHz for land and coastline were chosen to optimize the ability of the retrieval to compensate for possible errors in the land fraction within a footprint. Land fraction is supplied to the algorithm from a digital database. For open ocean, $\epsilon_0(\nu)$ is calculated from the Fresnel equations for a flat surface, using the double-Debye dielectric constant model of *Ellison et al.* [2003]; the values $s = 1.5$ and $\nu_1 = 50$ GHz were chosen to fit the frequency dependence of emissivity increases due to sea state found by *Rosenkranz* [1992].

[8] To find the values of T_0 , T_1 , and T_2 the retrieval needs the Jacobian matrix [see *Rosenkranz*, 2001, section IIIB] whose elements corresponding to these parameters are calculated, at any frequency, as partial derivatives

Table 1. Surface-Model Parameters Fixed by Classification ($\sigma_{0,1,2,p}$ = A Priori Standard Deviation of T_0 , T_1 , T_2 , p_p)

Type	Surface	s	ν_1 , GHz	ν_2 , GHz	σ_0 , K	σ_1 , K	σ_2 , K	σ_p
0	coastline ^a	1.2	90	...			0	0.12
1	land	1.2	90	...	15	20	0	0
2	water ^a	1.5	50	...			0	0.12
3	high-emissivity sea ice	3	40	120	10	10	10	0
4	low-emissivity sea ice	3	40	120	10	10	10	0
5	snow (high-frequency scattering)	3	50	150	20	20	20	0
6	glacier/snow (very low frequency scattering)	3	40	120	20	20	20	0
7	snow (low-frequency scattering)	3	33	90	20	20	20	0

^aFor water or coastline, $\sigma_0^2 = 25 + (0.55 T_s \sigma_L)^2$ and $\sigma_1^2 = 100 + (0.25 T_s \sigma_L)^2$, where σ_L is the estimated uncertainty in the land fraction.

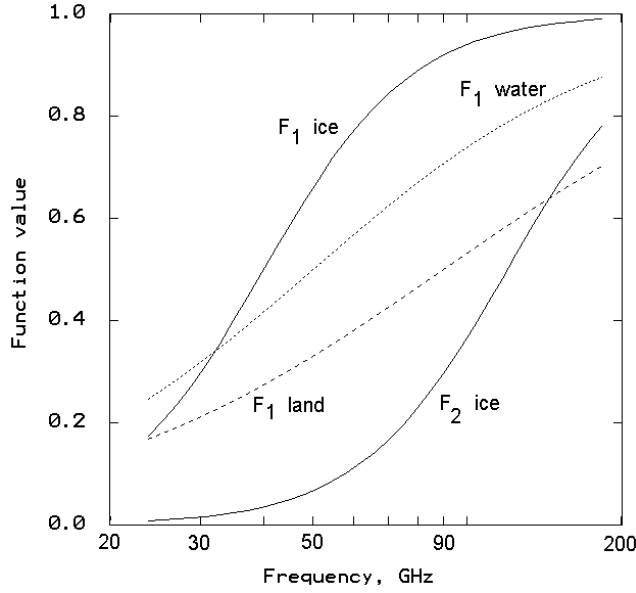


Figure 2. Functions $F_1(\nu)$ and $F_2(\nu)$ for surface types 0 or 1 (dashed line), 2 (dotted line), and 3, 4, or 6 (solid lines).

with other parameters including surface temperature held constant:

$$\frac{\partial T_B}{\partial T_0} = \frac{\partial T_B}{\partial T_{SB}} = \tau(1 - T_{Bsky}/T_S) \quad (4a)$$

$$\frac{\partial T_B}{\partial T_1} = \frac{\partial T_B}{\partial T_{SB}} F_1 \quad (4b)$$

$$\frac{\partial T_B}{\partial T_2} = \frac{\partial T_B}{\partial T_{SB}} F_2. \quad (4c)$$

3. Surface Scattering Model

3.1. Over Land and Ice

[9] When the surface is land (fraction > 0.5), snow, or sea ice, the downward propagating sky brightness temperature T_{Bsky} is calculated at an angle θ_{ref} from zenith that approximates the cosine-weighted brightness temperature corresponding to Lambertian surface scattering. In other words, for any atmospheric profile and sky opacity there is (by the mean value theorem) some angle θ_L at which $T_{Bsky}(\theta_L)$ is equal to the zenith-cosine-weighted average of T_{Bsky} over the upper hemisphere:

$$T_{Bsky}(\theta_L) = 2 \int_0^{\pi/2} T_{Bsky}(\theta) \cos(\theta) \sin(\theta) d\theta. \quad (5)$$

Figure 3 plots $\secant \theta_L$ for several frequencies versus zenith opacity, as the surface elevation is varied. These curves were found to be remarkably insensitive to the temperature profile. We wish to approximate θ_L by an analytic function θ_{ref} . Equating the cosine-weighted average of transmittance

to $\exp[-\kappa_0 \sec(\theta_{ref})]$, where κ_0 is the opacity of the atmosphere at zenith, results in [Mätzler, 1987, 2005]:

$$\secant \theta_{ref} = -\ln[2E_3(\kappa_0)]/\kappa_0, \quad (6)$$

in which $E_3()$ is the exponential integral of order 3. Equation (6) is plotted as the dash-dot line in Figure 3. The dashed line in Figure 3 shows the approximation used operationally in the forward algorithm,

$$\secant \theta_{ref} = 1.55 - 0.16 \ln(\kappa_0 + 0.06). \quad (7)$$

Use of (7) to calculate sky brightness temperature reproduces a cosine-weighted average sky brightness to within $\sim 1K$ for the AMSU and HSB frequencies.

3.2. Over Water

[10] For footprints over water or coastline surfaces, the downward propagating brightness temperature is calculated for zenith angle θ_{ref} , where

$$\secant \theta_{ref} = \rho \secant \theta, \quad (8)$$

and θ is the zenith angle for the upward propagation path from the surface footprint to the satellite. A similar approach has been applied to infrared radiance calculations by Nalli *et al.* [2001], who calculated θ_{ref} from a surface roughness model. In the present algorithm ρ is estimated as part of the retrieval solution. To be precise, the retrieval state vector includes a parameter p_ρ , and

$$\rho = 1 + \text{ramp}(p_\rho, 0.02), \quad (9)$$

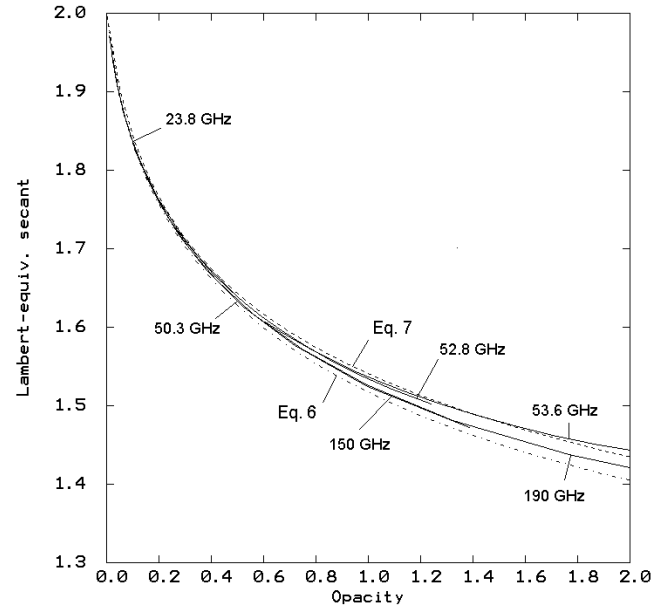


Figure 3. Effective secant for a Lambertian sky brightness temperature at various frequencies, compared with equations (6) and (7).

where

$$\text{ramp}(x, c) = \begin{cases} x & \text{for } x \geq c; \\ c \exp(x/c - 1) & \text{for } x < c. \end{cases} \quad (10)$$

The ramp function restricts ρ to values >1 and, because of its exponential knee, is differentiable everywhere, so that the Jacobian used in the retrieval solution is analytically calculable as

$$\frac{\partial T_B(\theta)}{\partial p_p} = \frac{\partial \rho}{\partial p_p} \sec(\theta)(1 - T_{SB}/T_S)\tau(\theta) \frac{\partial T_{Bsky}(\theta_{ref})}{\partial \sec(\theta_{ref})}. \quad (11)$$

[11] In principle, θ_{ref} should have some dependence on atmospheric opacity, though perhaps not as much as in the Lambertian case. However, for the sake of simplicity the same value of ρ is applied to all channels here. Retrieved values for ρ generally lie in the range 1.0–1.2, which is consistent with the theoretical calculations of *Guissard and Sobieski* [1994] for a wind-roughened sea surface at 50° incidence. It may be worth noting that an instrument that observed only in atmospheric windows would not be able to distinguish between a value of $\rho > 1$ and an increased atmospheric opacity due to clouds or the water vapor continuum. This degeneracy is lifted when the 50.3 GHz channel of AMSU-A is used in the retrieval, because the oxygen opacity is not a free variable.

[12] For water surfaces, the parameters T_0 , T_1 , and p_p are all related to roughness, and therefore the a priori statistics assigned to them assume correlation coefficients of 0.2. As indicated by the standard deviations in Table 1, at most three of the four surface roughness parameters are allowed to vary for any surface type.

4. Wind Speed Dependence of Surface Parameters Over Ocean

[13] The three ocean surface roughness parameters ρ , T_0 , and T_1 are used by the forward calculation to allow the retrieval to match observed brightness temperatures. We can validate them in the sense of showing that they correlate with near-surface wind speed, which is one of the most important physical variables determining ocean surface roughness. Friction velocity could also be used, but wind speed is more directly obtained from conventional sources. It is known that ocean surface emissivity depends also on wind direction; for example, at a 53° incidence angle, *Meissner and Wentz* [2002] found a directional variation of ± 1 K in 37-GHz surface brightness for wind speeds between 6 and 10 m/s. We did not subclassify our comparison data by wind direction, so this increases the scatter of the observations.

[14] The relation of ρ , T_0 , and $T_\infty (= T_0 + T_1 \text{ over ocean})$ to wind speed is shown in Figure 4 for 2207 observations in the latitude range 50S to 50N at scan angles within 9.5° of nadir on the days of 1 and 3 January 2003. Wind speed is the boundary layer (0 to 250m) average wind from NOAA's AVN model, interpolated spatially and temporally to the observations from 3-, 6-, and 9-hour forecasts. These

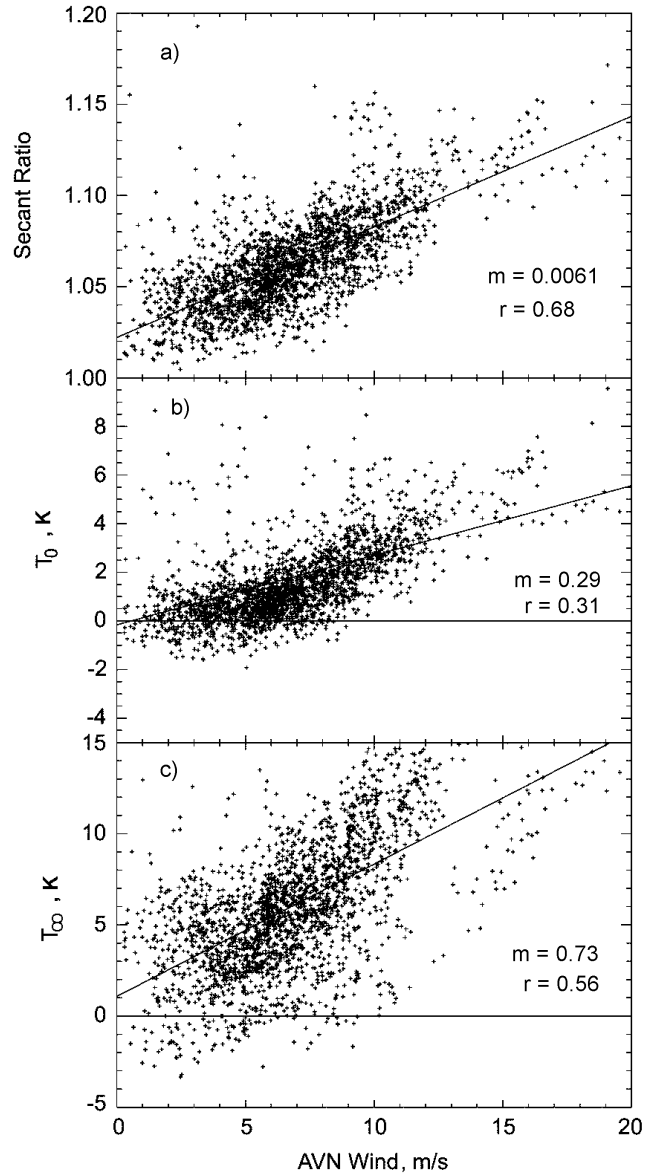


Figure 4. Retrieved values for near-vertical incidence over ocean of (a) the reflected/direct secant ratio ρ , (b) the low-frequency asymptote of the surface brightness adjustment T_0 , and (c) the high-frequency asymptote of the surface brightness adjustment T_∞ , versus near-surface wind speed; m is the slope of the regression line, and r is the correlation coefficient.

observations include both day and night cases, but they were selected, using AIRS data, for absence of clouds. The correlation coefficients of these three parameters with wind speed are given in Figure 4.

[15] As the magnitude of the scan angle increases beyond $\sim 20^\circ$, the slope of the regression line for ρ decreases, as seen in Figure 5. The sensitivities of T_0 and T_∞ to wind speed also seem to decrease slightly at larger scan angles, although that change may not be statistically significant. The effects of increasing incidence angle, polarization (which is vertical near nadir and rotates with scan angle) and increased atmospheric opacity are combined in Figure 5. Incidence

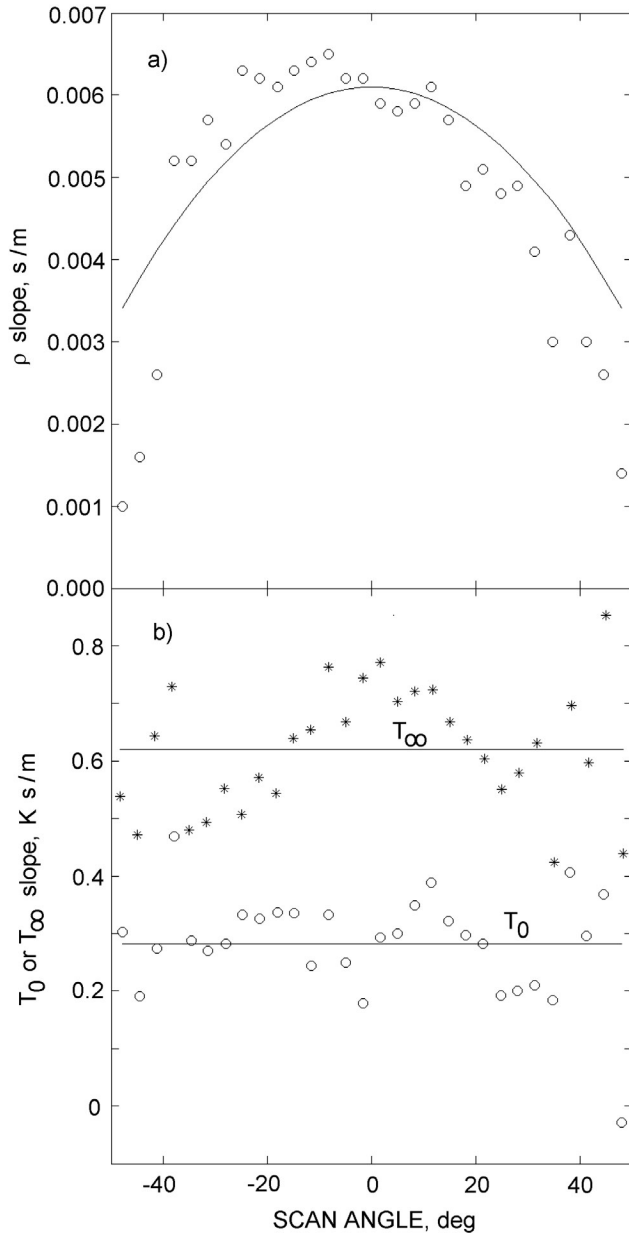


Figure 5. Regression line slopes for (a) ρ and (b) T_0 (circles) and T_∞ (asterisks) regressed against near-surface wind, as a function of scan angle.

angle θ at the earth's surface is related to the instrument scan angle ϕ by

$$\sin(\theta) = \sin(\phi)(R + A)/R, \quad (12)$$

where $R = 6371$ km is the radius of the earth and $A = 705$ km is the altitude of the Aqua satellite. Hence the maximum value of θ is 56° . The curve in Figure 5a is given by $0.0061 \cos(\theta)$, for which the difference

$$\sec(\theta_{\text{ref}}) - \sec(\theta) = (\rho - 1) \sec(\theta) \cong 0.0061 \cdot (\text{wind speed}) \quad (13)$$

is independent of θ . This curve fits the data over most of the range of measured angles. The horizontal lines in Figure 5b indicate mean values of the data.

[16] Figures 4 and 5 show that the sensitivity of T_∞ to wind exceeds that of T_0 . (In other words, T_1 is usually positive.) These results are consistent with those obtained from SSM/I measurements [Rosenkranz, 1992; Meissner and Wentz, 2003], where the wind speed sensitivity of H-pol emissivity at 53° incidence was found to increase steadily with frequency up to at least 85 GHz (the highest frequency observed by SSM/I), and also with earlier observations covering the range of 1.4 to 37 GHz [Wentz, 1983; Sasaki et al., 1987]. (For AMSU-A, an incidence angle of 52° corresponds to a scan angle of 45° , where the instrument receives equal fractions of H- and V-polarization.) The retrieval algorithm finds some variability in the frequency dependence of rough ocean emissivity, however. The measured correlation coefficient between T_0 and T_1 is significantly less than unity; 0.36 for the data in Figure 4, for example. That variability could be the result of processes that depend on geophysical variables other than wind speed (such as wind direction and fetch), nonlinearities of the processes, measurement errors, or approximations made in the forward model.

[17] A rather sensitive test of the forward model is the extent to which it suppresses crosstalk from surface emissivity and roughness to other parameters, such as surface

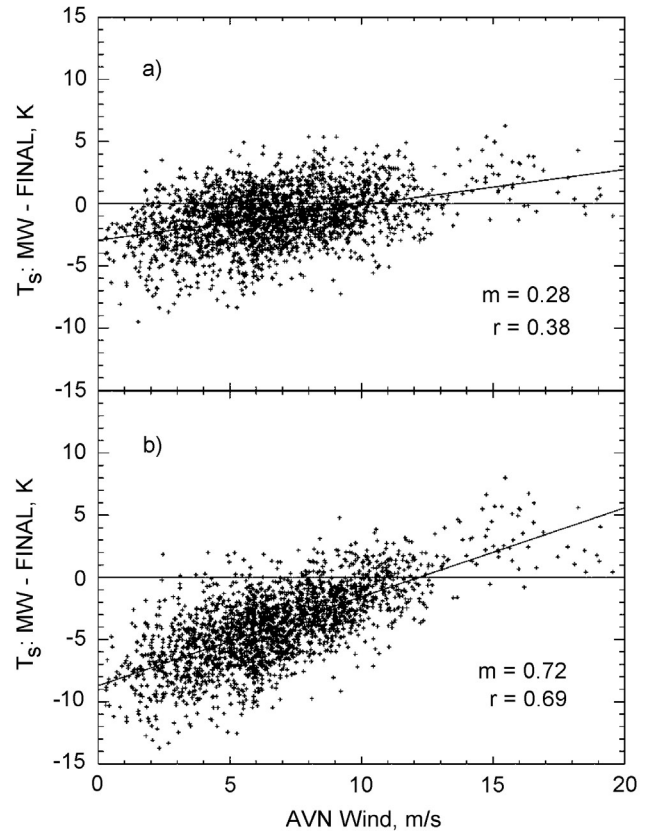


Figure 6. As in Figure 4 but for the difference between retrieved surface temperatures from the microwave-only and the infrared retrieval stages: (a) with estimation of ρ and (b) without estimation of ρ .

Table 2. Observed^a T_A – Calculated^b T_B for HSB, Using ARM-SGP RS-90 Sondes

Channel	Frequency, GHz	N	Mean(obs-calc), K	σ (obs-calc), K
HSB 3	183.3 \pm 1	88	–0.82, –0.83	2.16, 2.15
HSB 4	183.3 \pm 3	87	–0.53, –0.39	1.43, 1.43
HSB 5	183.3 \pm 7	69	–0.48, –0.34	1.50, 1.50

^aSelected to minimize distance from site.^bNormal font numbers: using rapid algorithm; italics: using line-by-line algorithm.

temperature. The lowest temperature-sounding channel, AMSU4 at 52.8 GHz, has significant contributions from the surface and reflected atmosphere. Therefore the temperature retrieval depends on accurate estimation of surface brightness and scattering. Figure 6a shows the difference between the surface skin temperatures retrieved in the microwave-only stage and the final retrieval stage, where AIRS infrared data are used, plotted versus wind speed for the same cases as Figure 4. The regression line has a small slope of 0.28 K/(m/s), which shows that the surface temperature retrieved from the microwave measurements has some residual influence from surface roughness. For the previous version of the algorithm, in which ρ was fixed at 1.1 for the temperature channels, that slope was 0.72, as seen in Figure 6b. The RMS differences of surface temperature are 2.4 K and 4.9 K, respectively, in the two cases. Thus we find that the undesirable crosstalk between surface roughness and temperature is reduced by allowing ρ to be a variable, although the current model has not entirely eliminated it. For scan angles increasing above $\sim 20^\circ$ (not shown), the dependence of retrieved surface temperature on wind speed decreases, becoming slightly negative (-0.1) toward the ends of the scan in both versions of the algorithm.

5. Comparisons of HSB Observations to Calculations From In Situ Measurements

[18] For many of the AMSU-A channels, at the largest scan angles as much as $\sim 1\%$ of their integrated antenna directivity lies in sidelobes that are directed at cold space rather than the earth. The resulting biases in the observations are compensated in the retrieval algorithm by a “tuning” correction which currently is derived by comparison of antenna temperatures observed from cloud-free ocean footprints with model-calculated brightness temperatures. These corrections, which depend on scan position, are currently applied during the retrieval to AMSU-A channels 1–14. Since the sidelobe effects are significant, comparison of forward model calculations with observed

antenna temperatures is not a particularly meaningful test of the forward model for these channels. However, in R03 the forward model was validated in the oxygen band using NOAA 15 AMSU-A observations with sidelobe corrections calculated by *Mo* [1999] from antenna range measurements. The mean differences between the corrected observations and calculations based on radiosondes ranged from -0.42 to $+0.23$ K for six AMSU channels, with standard deviations less than 0.8 K except for the lowest-altitude channel.

[19] HSB [*Lambrigtsen and Calheiros*, 2003], on the other hand, is a near copy (with one channel deleted) of AMSU-B, for which antenna measurements [*Hewison and Saunders*, 1996] showed very low sidelobe levels at far angles. Those measurements indicate that at the frequencies that AMSU-B has in common with HSB, the contribution of cold space to integrated directivity varies from essentially zero at scan positions near the center to at most 0.2% at large angles (T. Hewison, private communication, 1998). Antenna pattern measurements were not made for HSB, but the data discussed below show that it also has low sidelobe levels; therefore tuning corrections are not currently applied to any of the HSB channels. Antenna temperatures measured by these channels are compared below to forward model calculations based on profiles measured in situ by radiosondes. The HSB channels are numbered 2 through 5 for consistency with AMSU-B. The RMS sensitivities of the four channels are 0.68, 0.57, 0.39, and 0.30 K, respectively, in one integration period.

[20] *Buehler et al.* [2004] compared AMSU-B measurements to calculations based on radiosondes launched at Lindenberg, Germany. They found systematic differences only for the 183 ± 1 GHz channel, which they attributed to radiosonde humidity measurements of 0% in the upper troposphere when the true relative humidity was believed to be 4%.

[21] Tables 2 and 3 show comparisons of HSB measurements (T_A) with our calculations (T_B) based on the “best estimate” profiles from special radiosonde launches [see *Tobin et al.*, 2006] coincident with Aqua satellite overpasses at two of the Atmospheric Radiation Measurement sites, Southern Great Plains and Nauru Island (Tropical Western Pacific). These radiosondes had a humidity sensor of a more modern design than the radiosondes used by *Buehler et al.* The technique applied by *Tobin et al.* to the ARM-site sondes includes scaling the humidity profile to match a simultaneous measurement of integrated water vapor by a ground-based microwave radiometer. *Miloshevich et al.* [2006] found a diurnal variation in RS-90 sonde humidity measurements; however, the scaling removes this variation, amounting to a few percent, for the total integrated water

Table 3. Observed^a T_A – Calculated^b T_B for HSB, Using ARM-TWP RS-90 Sondes

Channel	Frequency, GHz	N	Mean(obs-calc), K	σ (obs-calc), K
HSB 2	150	31	–0.56, –0.55	1.13, 1.13
HSB 3	183.3 \pm 1	32	–0.55, –0.53	1.03, 1.03
HSB 4	183.3 \pm 3	32	–0.55, –0.41	0.63, 0.63
HSB 5	183.3 \pm 7	32	–0.65, –0.51	0.89, 0.88

^aSelected to minimize distance from site.^bNormal font numbers: using rapid algorithm; italics: using line-by-line algorithm.**Table 4.** Observed^a T_A – Calculated^b T_B for HSB, Using Chilled Mirror Sondes

Channel	Frequency, GHz	N	Mean(obs-calc), K	σ (obs-calc), K
HSB 3	183.3 \pm 1	32	–0.37, –0.37	1.26, 1.26
HSB 4	183.3 \pm 3	30	–0.25, –0.11	0.94, 0.91
HSB 5	183.3 \pm 7	27	–0.21, –0.09	0.59, 0.57

^aWithin 40 km of launch site, selected to minimize $(\text{distance}/50\text{km})^2 + (\text{landfrac}/0.1)^2$.^bNormal font numbers: using rapid algorithm; italics: using line-by-line algorithm.

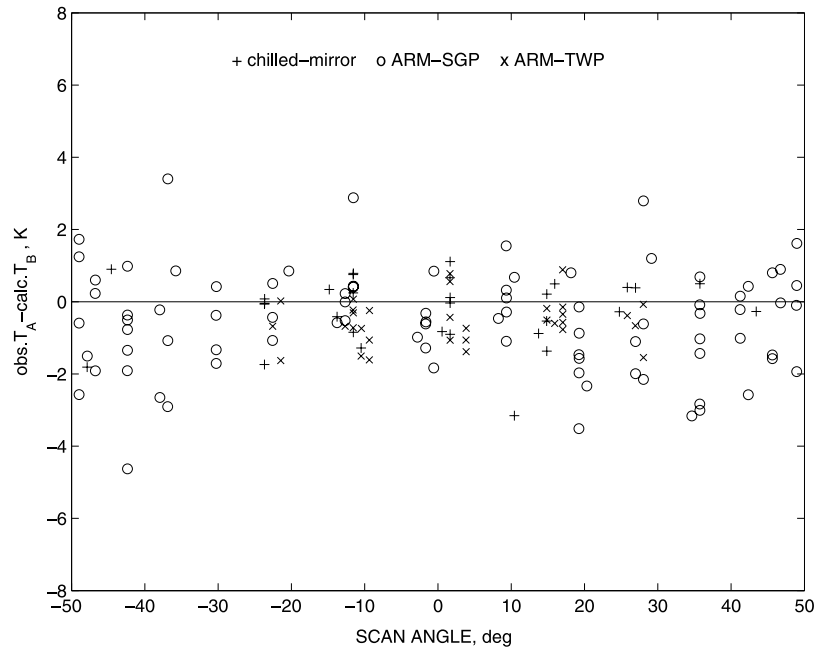


Figure 7. Observed T_A minus calculated T_B for HSB channel 4 versus scan angle.

vapor. There may still remain a diurnally varying bias in the upper troposphere. We did not classify our comparisons by time of day, so it is possible that diurnal variation contributes a small amount to the standard deviations, although most of the emission measured by even the HSB channel closest to the water line comes from layers of the atmosphere below ~ 300 hPa.

[22] Table 4 shows our comparisons with a special campaign of sonde launches with the Cryogenic Frostpoint Hygrometer, the characteristics of which are described by *Miloshevich et al.* [2006], at a wide latitudinal range of locations (Galapagos Is., Hawaii, Alabama, Colorado, and Finland). These soundings are not scaled.

[23] The HSB channels are near a water vapor line, and special launches are necessary in order to avoid time and spatial errors due to the variability of water vapor. Each sounding is matched with one HSB footprint, selected as noted in the tables. The forward calculations were done in two ways: first, using the surface model described in sections 2 and 3, which contains parameters retrieved from the measurements; second, with a “default” assumption of smooth specular surface for the part of the footprint covered by water, and unit emissivity for the part covered by land. The results presented are for the full surface model, but since our purpose in this section is to test the atmospheric transmittance part of the forward model, the tables include channels only when the mean difference between the full surface model and the default model is less than 1 K. (The largest difference for the data shown in the tables was actually 0.4 K.) Individual profiles were also screened to exclude those with precipitable water less than 1, 5, and 15 mm for channels 3, 4, and 5 respectively, in order to minimize surface contributions. A detailed description of the atmospheric transmittance algorithm is given in R03. The calculations were also done using a line-by-line algorithm with three-point integration by Simpson’s rule over each passband, giving the results in italics in Tables 2–4.

[24] The forward calculations did not include any cloud liquid water absorption; however, footprints for which the total cloud liquid exceeded 0.1 mm were excluded from the comparison. At the ARM sites, cloud liquid was obtained from ground-based radiometers; elsewhere, the value retrieved from AMSU and HSB [see *Rosenkranz*, 2006] was used for this screening purpose. In addition, three outlier points, possibly due to precipitation not seen by the ground radiometers, were excluded from the statistics of Tables 2 and 3; these had observed-calculated differences of -17 and -33 K, respectively, for HSB4 and HSB5 from one profile (23 July 2003) at the ARM-SGP site, and -7 K for HSB2 from one profile (20 January 2003) at the ARM-TWP site.

[25] Tables 2–4 show agreement ranging from 0.2 K to 0.8 K in the means, and 0.6 K to at worst 2.2 K for standard deviations. In general, the standard deviations increase with altitude (i.e., channels closer to the line center), which is consistent with known difficulties in radiosonde measurement of water vapor at low temperatures. Any spectroscopic errors would be expected to have a mean component, since they are systematic. For example, a uniform change of 5% in water vapor absorption coefficient would cause a change of typically 0.3 to 0.5 K in computed HSB brightness temperatures. However, the mean errors obtained are smaller than the 1 K specification for absolute calibration accuracy of the instrument. One known contribution to the differences in Tables 2–4 is that the calculations for HSB3 are on average a few tenths of a degree too warm because of neglecting the effect of two ozone lines at 184.38 and 184.75 GHz. Averaged over the passband of that channel, the ozone lines depress the brightness temperature by ~ 0.2 K near nadir to ~ 0.5 K at the ends of the scan [*John and Buehler*, 2004].

[26] The observed minus calculated (rapid algorithm) differences for the 183 ± 3 GHz channel are plotted versus scan angle in Figure 7. There is no evident dependence on

angle, which confirms that sidelobe effects are small for the HSB.

[27] We did similar comparisons using the standard synoptic radiosondes that are launched from many sites around the earth. Those comparisons yielded standard deviations of 4.3, 2.9 and 2.4 K for HSB channels 3 to 5. These larger deviations show the need for high-quality in situ measurements when validating radiometric data in water vapor bands.

6. Conclusions

[28] The influence of surface scattering on window channel brightness temperatures was found to be significant, and was included in the forward model. The model has several parameters to describe the surface emissivity and scattering characteristics; some of these are assigned by a preliminary classification of surface type, while others (at most three) are retrieved simultaneously with atmospheric moisture variables. Over ocean, the two variables describing surface emissivity and the single variable describing surface scattering are correlated with near-surface wind speed, as expected. The inclusion of these variables in the retrieval solution reduces the undesired influence of surface roughness on retrieved temperature, which indicates that they contribute to realistic modeling of the radiative transfer physics. Future work will be directed toward further reduction of residual modeling errors.

[29] The HSB matchups and calculations based on special research-quality radiosondes confirm the accuracy of the rapid transmittance algorithm, which was derived from laboratory absorption measurements. In combination with the previous tests in R03 of AMSU-A transmittances, the results indicate that errors in calculated sounding channel transmittances are smaller than the calibration accuracy specifications for these two instruments.

[30] **Acknowledgments.** The efforts of the AIRS validation team in providing high-quality radiosonde profiles are gratefully acknowledged. This work was supported by NASA under contracts NAS5-31376 and NNG04HZ51C.

References

- Aumann, H. H., et al. (2003), AIRS/AMSU/HSB on the Aqua mission: Design, science objectives, data products, and processing systems, *IEEE Trans. Geosci. Remote Sens.*, *41*, 253–264.
- Buehler, S. A., M. Kuvshinov, V. O. John, U. Leiterer, and H. Dier (2004), Comparison of microwave satellite humidity data and radiosonde profiles: A case study, *J. Geophys. Res.*, *109*, D13103, doi:10.1029/2004JD004605.
- Ellison, W. J., S. J. English, K. Lamkaouchi, A. Balana, E. Obligis, G. Deblonde, T. J. Hewison, P. Bauer, G. Kelly, and L. Eymard (2003), A comparison of ocean emissivity models using the Advanced Microwave Sounding Unit, the Special Sensor Microwave Imager, the TRMM Microwave Imager, and airborne radiometer observations, *J. Geophys. Res.*, *108*(D21), 4663, doi:10.1029/2002JD003213.
- Grody, N., F. Weng, and R. Ferraro (2000), Application of AMSU for obtaining hydrological parameters, in *Microwave Radiometry and Remote Sensing of the Earth's Surface and Atmosphere*, edited by P. Pampaloni and S. Paloscia, pp. 339–352, Brill Acad., Leiden, Netherlands.
- Guissard, A., and P. Sobieski (1994), A simplified radiative transfer equation for application in ocean microwave remote sensing, *Radio Sci.*, *29*, 881–894.
- Hewison, T. J., and R. Saunders (1996), Measurements of the AMSU-B antenna pattern, *IEEE Trans. Geosci. Remote Sens.*, *34*, 405–412.
- John, V. O., and S. A. Buehler (2004), The impact of ozone lines on AMSU-B radiances, *Geophys. Res. Lett.*, *31*, L21108, doi:10.1029/2004GL021214.
- Karbou, F., C. Prigent, L. Eymard, and J. R. Pardo (2005), Microwave land emissivity calculations using AMSU measurements, *IEEE Trans. Geosci. Remote Sens.*, *43*, 948–959.
- Lambrigtsen, B. H., and R. V. Calheiros (2003), The humidity sounder for Brazil—An international partnership, *IEEE Trans. Geosci. Remote Sens.*, *41*, 352–361.
- Mätzler, C. (1987), Applications of the interaction of microwaves with the natural snow cover, *Remote Sens. Rev.*, *2*(2), 259–392.
- Mätzler, C. (2005), On the determination of surface emissivity from satellite observations, *IEEE Geosci. Remote Sens. Lett.*, *2*, 160–163.
- Meissner, T., and F. Wentz (2002), An updated analysis of the ocean surface wind direction signal in passive microwave brightness temperatures, *IEEE Trans. Geosci. Remote Sens.*, *40*, 1230–1240.
- Meissner, T., and F. Wentz (2003), A radiative transfer model function for 85.5 GHz Special Sensor Microwave Imager ocean brightness temperatures, *Radio Sci.*, *38*(4), 8066, doi:10.1029/2002RS002655.
- Miloshovich, L. M., H. Vömel, D. N. Whiteman, B. M. Lesht, F. J. Schmidlin, and F. Russo (2006), Absolute accuracy of water vapor measurements from six operational radiosonde types launched during AWEX-G, and implications for AIRS validation, *J. Geophys. Res.*, doi:10.1029/2005JD006083, in press.
- Mo, T. (1999), AMSU-A antenna pattern corrections, *IEEE Trans. Geosci. Remote Sens.*, *37*, 103–112.
- Nalli, N. R., W. L. Smith, and B. Huang (2001), Quasi-specular model for calculating the reflection of atmospheric-emitted infrared radiation from a rough water surface, *Appl. Opt.*, *40*, 1343–1353.
- Rosenkranz, P. W. (1992), Rough-sea microwave emissivities measured with the SSM/I, *IEEE Trans. Geosci. Remote Sens.*, *30*, 1081–1085.
- Rosenkranz, P. W. (2001), Retrieval of temperature and moisture profiles from AMSU-A and AMSU-B measurements, *IEEE Trans. Geosci. Remote Sens.*, *39*, 2429–2435.
- Rosenkranz, P. W. (2003), Rapid radiative transfer model for AMSU/HSB channels, *IEEE Trans. Geosci. Remote Sens.*, *41*, 362–368.
- Rosenkranz, P. W. (2006), Cloud liquid-water profile retrieval algorithm and validation, *J. Geophys. Res.*, *111*, D09S08, doi:10.1029/2005JD005832.
- Sasaki, Y., I. Asanuma, K. Muneyama, G. Naito, and T. Suzuki (1987), The dependence of sea-surface microwave emission on wind speed, frequency, incidence angle, and polarization over the frequency range from 1 to 40 GHz, *IEEE Trans. Geosci. Remote Sens.*, *25*, 138–146.
- Tobin, D. C., H. E. Revercomb, R. O. Knuteson, B. M. Lesht, L. L. Strow, S. E. Hannon, W. F. Feltz, L. A. Moy, E. J. Fetzer, and T. S. Cress (2006), Atmospheric Radiation Measurement site atmospheric state best estimates for Atmospheric Infrared Sounder temperature and water vapor retrieval validation, *J. Geophys. Res.*, doi:10.1029/2005JD006103, in press.
- Tretyakov, M., V. V. Parshin, M. A. Koshelev, V. N. Shanin, S. E. Myasnikova, and A. F. Krupnov (2003), Studies of 183 GHz water line: Broadening and shifting by air, N₂ and O₂ and integral intensity measurements, *J. Mol. Spectrosc.*, *218*, 239–245.
- Weng, F., B. Yan, and N. C. Grody (2001), A microwave land emissivity model, *J. Geophys. Res.*, *106*, 20,115–20,123.
- Wentz, F. J. (1983), A model function for ocean microwave brightness temperatures, *J. Geophys. Res.*, *88*, 1892–1908.

C. D. Barnett, National Environmental Satellite Data and Information Service, NOAA, Camp Springs, MD 20746, USA.

P. W. Rosenkranz, Research Laboratory of Electronics, Massachusetts Institute of Technology, Cambridge, MA 02139, USA. (pwr@mit.edu)